Hexahedron Prism-Anchored Octahedronal CeO$_2$: Crystal Facet-Based Homojunction Promoting Efficient Solar Fuel Synthesis

Ping Li,[‡,§] Yong Zhou,*[,†,‡,§,∥] Zongyan Zhao,[⊥] Qinfeng Xu,[‡] Xiaoyong Wang,[‡] Min Xiao,[‡] and Zhigang Zou*[,†,‡,§,∥]

[†]Key Laboratory of Modern Acoustics (MOE), Institute of Acoustics, Department of Physics, [‡]National Laboratory of Solid State Microstructures, School of Physics, [§]Eco-Materials and Renewable Energy Research Center (ERERC), [∥]Collaborative Innovation Center of Advanced Microstructures, Nanjing University, Nanjing 210093, China

[⊥]Faculty of Materials Science and Engineering, Key Laboratory of Advanced Materials of Yunnan Province, Kunming University of Science and Technology, Kunming 650093, China

S Supporting Information

ABSTRACT: An unprecedented, crystal facet-based CeO$_2$ homojunction consisting of hexahedron prism-anchored octahedron with exposed prism surface of {100} facets and octahedron surface of {111} facets was fabricated through solution-based crystallographic-oriented epitaxial growth. The photocatalysis experiment reveals that growth of the prism arm on octahedron allows to activate inert CeO$_2$ octahedron for an increase in phototocatalytic reduction of CO$_2$ into methane. The pronounced photocatalytic performance is attributed to a synergistic effect of the following three factors: (1) band alignment of the {100} and {111} drives electrons and holes to octahedron and prism surfaces, respectively, aiming to reach the most stable energy configuration and leading to a spatial charge separation for long duration; (2) crystallographic-oriented epitaxial growth of the CeO$_2$ hexahedron prism arm on the octahedron verified by the interfacial lattice fringe provides convenient and fast channels for the photogenerated carrier transportation between two units of homojuntion; (3) different effective mass of electrons and holes on {100} and {111} faces leads to high charge carrier mobility, more facilitating the charge separation. The proposed facet-based homojunction in this work may provide a new concept for the efficient separation and fast transfer of photoinduced charge carriers and enhancement of the photocatalytic performance.

The photocatalytic activity not only strictly depends on the inherent physical properties of photocatalysts but also is tightly correlated to the exposure of external crystal surface, especially, the surface atomic arrangement and construction.[1] Surface energy levels (namely, surface electronic structures) of the conduction bands (CB) and valence bands (VB) of different surface facets are distinct so that photoexcited holes and electrons will diffuse from the bulk toward the surface before recombination and are trapped by the topmost exposed atoms, which leads to the efficient separation. Largely inspired by the rapid development of crystal engineering of faceted TiO$_2$,[2] BiVO$_4$,[3] Cu$_2$O,[4−6] Ag$_3$PO$_4$,[7−9] BiOCl,[10,11] and so on, the controllable development of crystal facets is becoming an energetic prospect for efficient artificial photosynthesis. While most crystal facet engineering of semiconductor photocatalysts reported so far was designed in single polyhedron particles, the photoinduced carries closely trapped to only one unit still possibly suffer from a substantially increasing chance of consumption by bulk and surface recombination.[12,13]

The homojunction (such as phase homojunction) is the junction layers built from the same semiconductor materials.[14,15] An internal field generated from different alignment of band edges between two parts could facilely restrain the photoinduced carrier recombination. Relative to heterojunctions made of two different compositions, the fact that the same component on both sides of the homojunction interface renders continuity of the band bonding promotes that the photoexcited charge carriers transfer across the interface. CeO$_2$-based materials have been widely explored for their application in organic catalysis,[16,17] photocatalystic water splitting and photodegradation of organic contamination.[18,19] A solar-driven catalysis over CeO$_2$ at elevated temperatures thermochemically dissociates CO$_2$ and H$_2$O, yielding CO and H$_2$, respectively.[20] Different crystal planes of ceria {111}, {110}, and {100} exhibit different catalysis properties such as surface stability,[21,22] oxygen vacancy formation energy,[18] and interaction with surface molecules.[23]

Herein, we report an unprecedented, crystal facet-based CeO$_2$ homojunction consisting of hexahedron prism-anchored octahedron with exposed prism surface of {100} facets and octahedron surface of {111} facets through solution-based crystallographic-oriented epitaxial growth. The photocatalysis experiment reveals that growth of the prism arm on octahedron allows to activate inert CeO$_2$ octahedron for an increase in photocatalytic reduction of CO$_2$ into methane. The pronounced photocatalytic performance is attributed to a synergistic effect of the following three factors: (1) band alignment of the {100} and {111} drives the electron and hole to octahedron and prism surfaces, respectively, aiming to reach the most stable energy configuration and leading to a spatial charge separation for long duration; (2) crystallographic-oriented epitaxial growth of the CeO$_2$ hexahedron prism arm on the octahedron verified by the interfacial lattice fringe provides convenient and fast channels for

the photogenerated carrier transportation between two units of homojuntion; (3) different effective mass of electrons and holes on {100} and {111} faces leads to high charge carrier mobility, more facilitating the charge separation. The proposed facet-based homojunction in this work may provide a new concept for the efficient separation and fast transfer of photogenerated charge carriers and enhancement of the photocatalytic efficiency.

Phosphate ions ($H_2PO_4^-$) as a mineralizer make a prominent role in the growth of the hexahedron prism anchored-octahedral morphology of the CeO_2.[24] The FE-SEM images display that the CeO_2 (the product is referred to as CP0) produced in the absence of $H_2PO_4^-$ predominately (99%) exhibits regular octahedron morphology with uniform edge size of ~450 nm and smooth surface (Figure 1a). With addition of 0.5% $H_2PO_4^-$,
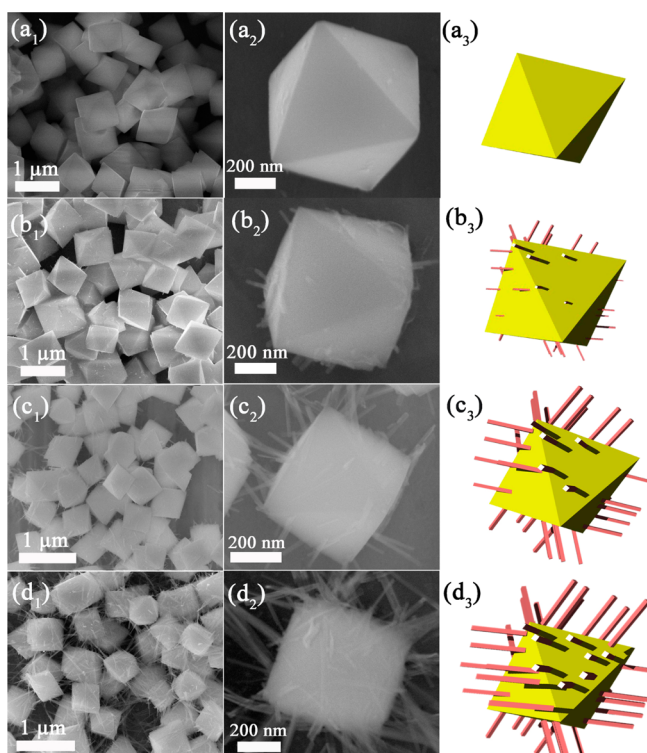

Figure 1. SEM images of CeO_2: (a_1,a_2) CP0; (b_1,b_2) CP1; (c_1,c_2) CP2; (d_1,d_2) CP3; and schematic of CP0 (a_3), CP1 (b_3), CP2 (c_3), and CP3 (d_3).

the octahedron surface was sporadically textured with nanorod-like arm of ~200 nm in length (Figure 1b) (referred to CP1). The arms become denser, longer, and thicker with the concentration increase of $H_2PO_4^-$ to 1% and 2% (referred to CP2 and CP3, respectively) (Figure 1c,d). The octahedron core does not change in both morphology and size in the presence of $H_2PO_4^-$. The high-resolution FE-SEM image shows that those arms nearly perpendicularly protrude from the octahedron (see Figure 1c_2). The well-assembled orientation decorated on the octahedron implies that the arm nucleates on the surface of the octahedron and subsequently grows out of it. According to the classical nucleation theory, the growth process of the hierarchical CeO_2 structure is believed to be a two-step nucleation,[25] i.e., separated nucleation site and successive time for the growth of the octahedron and arm. The extended time and space involved in this two step nucleation, which is important to influence the shape of crystals, might offer more opportunities to govern the overall crystallization process by altering the reaction parameters,

which enables the crystal growth to proceed favorably along specific directions. The evolution of the present arm might be attributed to the $H_2PO_4^-$ as growth-controlling agent by absorbing the octahedron surface, which terminates the growth of octahedron morphology and allows the second nucleation site of one-dimensional orientation growth of the precursor. The similar mediation mechanism of phosphate ions was also feasible to govern the growth of {001}-terminated hematite Fe_2O_3 nanodisc using the phosphate ions as structure directing agent preferentially adsorbed on {110}.[26]

The transmission electron microscopy (TEM) image of the CP2 clearly shows the hexagonal and tetragonal projects of the prism anchored-octahedron taken by focusing the electron beam along one of the triangular faces and apex angles of the octahedron along the [001] crystallographic direction, respectively (Figure 2a−c). The lattice fringe spacing is measured 0.318
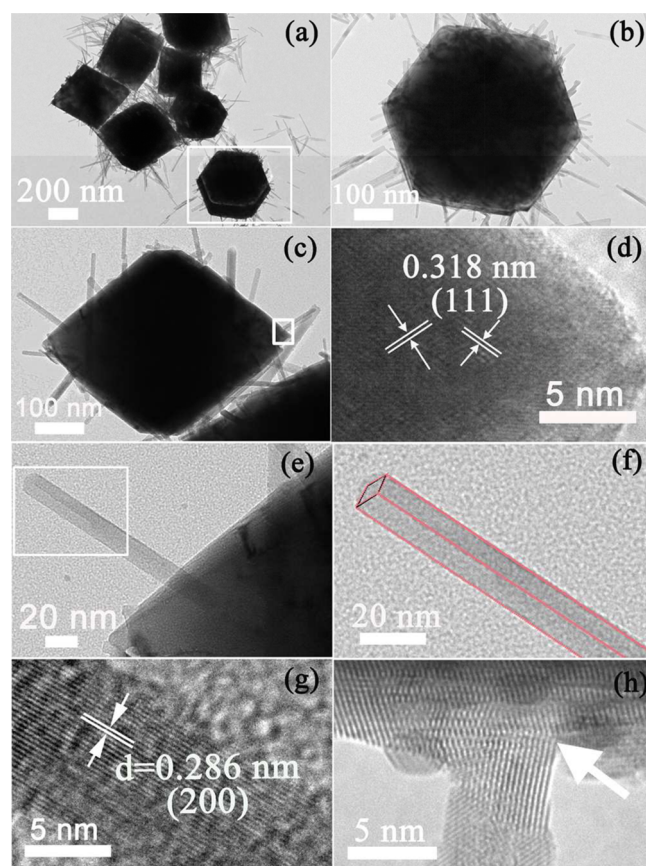

Figure 2. TEM images of hexahedron prism anchored octahedronal CeO_2 (CP2) (a−c,e,f); HRTEM images (d,g) derived from rectangles of panels c and e, respectively; HRTEM image of the CeO_2 hexahedron prism arm and the octahedron interface (h).

nm, which matches well with the (111) panels (Figure 2d). It indicates that these near-perfect octahedral morphology terminates eight {111} facets, being of the highest surface density of atoms and the lowest surface energy for body-centered cubic structured CeO_2.[27,28] The higher growth rate of {100} than {111} is thought to be responsible for the generation of the octahedral microcrystal.[29] The magnified TEM image confirms that the protruded arm with 10−15 nm width displays pronounced hexahedron prism with distinct ridge and lateral surface (Figure 2e and 2f). The crystal lattice pitches of the hexahedron prism with longitudinal direction are measured

0.286 nm, corresponding to (200) panels (Figure 2g), the four major exposed surfaces of the hexahedron prism determinable to be {100} facet. Interfacial crystal lattice match between the forming basal facets of the octahedron and hexahedron prism proves crystallographic-oriented epitaxial nucleation and growth of the tetragonal prism on the octahedron (Figure 2h). Therefore, the potential merits of applying building blocks with well developed facets for the present homojunction are a more intimate contact, which provides a convenient and fast channel for the photogenerated carrier transportation.

The X-ray diffraction (XRD) patterns clearly show that all the diffraction peaks of the CP2 could be well indexed to the body-centered cubic structure of CeO_2 (JCPDS no. 34-0394) (Figure S1), and no other phase is observed. The UV−vis absorption spectra suggest that the morphology change of CeO_2 has no effect on the onsets of the absorption edge (Figure S2), which is generally located at ca. 400 nm, consistent with the reported bandgap of CeO_2 (~3.1 eV).[30]

Photocatalytic reduction of CO_2 into solar fuels is based on the simulation of natural photosynthesis in green plants, producing O_2 and carbohydrates from CO_2 and H_2O employing sunlight as energy source.[31−35] H_2O is oxidized by the photogenerated holes in valence band to generate hydrogen ions via the reaction of $H_2O \rightarrow 1/2O_2 + 2H^+ + 2e^-$ (E°_{redox} = 0.82 V vs NHE); CO_2 is reduced by the photogenerated electrons in conduction band to CH_4 via the reaction of $CO_2 + 8e^- + 8H^+ \rightarrow CH_4 + 2H_2O$ (E°_{redox} = −0.24 V vs NHE). The photocatalytic CH_4 generation performance for the CO_2 reduction of the present CeO_2 homojunction with 0.5 wt % Pt cocatalyst loaded was investigated in Figure 3a. Not any CH_4 or any other hydrocarbon
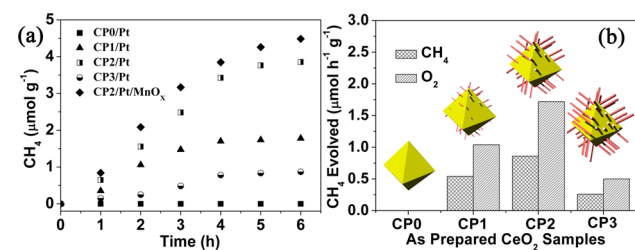

Figure 3. Specific CH_4 evolution activities of CP0, CP1, CP2, and CP3 (0.5% wt Pt, 0.5% wt MnO_x loaded) (a); CH_4 and O_2 generation rate of CP0, CP1, CP2, and CP3 with 0.5% wt Pt loaded (b).

species product were detected for the CP0, which is possibly due to rapid recombination of the photogenerated electron and hole on terminated {111}. However, the hexahedron prism-anchored octahedron displayed obvious photocatalytic activities with continuous light irradiation. The CP1 exhibited the CH_4 generation rate of 0.54 μmol h^{-1} g^{-1}, and further increases by 60% to 0.86 μmol h^{-1} g^{-1} for CP2 with more hexahedron prism arms (Figure 3b). Photodeposition of MnO_x oxide for CP2 further improves photocatalytic activity with 1.12 μmol h^{-1} g^{-1} CH_4 generation. Contrarily, the CH_4 generation rate of CP3 decreases to 0.26 μmol h^{-1} g^{-1} with further abundant arms. The excessive abundance of the hexahedron prism arms may decrease the number of the reduction sites on {111} negatively on photocatalytic efficiency. It indicates that an optimum ratio of the high-energy {100} oxidative facets to low-energy {111} reductive ones is essential to greatly decrease the charge recombination and thus improve photocatalytic CO_2 reduction activity of CeO_2. The quantum yield of CO_2 photoreduction was determined to be maximum 0.2% at 380 nm using monochromatic light and

monitoring the generation of CH_4 (Figure S3). The O_2 production has also been detected with about 2:1 molar ratio of O_2 to CH_4 (Figure 3b). Similar dependence of photoreduction yield of CO_2 into CH_4 on the ratio of different facets was also reported for TiO_2 polyhedron.[36] The identical CO_2 reduction experiments operated in the absence of light or photocatalysts display no appearance of product, demonstrating that the CO_2 reduction reaction occurs under light over the photocatalysts. Control experiments under UV−vis light irradiation were also performed over the photocatalysts in Ar atmosphere. In absence of CO_2, neither CH_4 nor other carbon compounds were detected, implying that there were no residual carbons in the system.

A cooperative mechanism is proposed to elucidate the differences in photocatalytic reactivity of the present CeO_2-based photocatalysts, concerning both favorable surface atomic structures and surface electronic structures. First, photocatalytic activity is strongly influenced by the energy position of the maximum of the VB and the minimum of the CB. Based on the different surface electronic structures of CeO_2 {111} and {100}, the density of states (DOS) shows the surface energy levels of CB and VB are more positive for {100} than {111}, corresponding to the Fermi energy entering the VB (Figure 4a). A slight difference
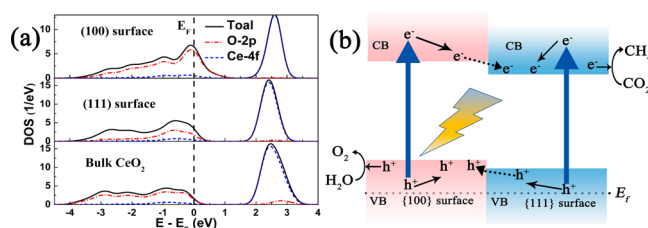

Figure 4. (a) Density of states (DOS) plots for {100} and {111} surface of cubic CeO_2 and bulk CeO_2. (b) Illustration of charge transfer cross {001} and {111} surface homojunction.

in energy of the VB and CB between {100} and {111} facets suggests that the hexahedron prism and octahedron can form a homojunction (Figure 4b). Electron transfer from {100} to {111} facets in CB and the hole transfer in the opposite direction in the VB is thus feasible thermodynamically, leading to the accumulation of electrons and holes separately on the {111} preferred as reduction sites and {100} as oxidation sites, respectively. The spontaneous charge transfer in the {100}/{111} facets increases both the yield and lifetime of charge carriers. The photoluminescence decay profiles demonstrate that the average decay time of the bare octahedron (CP0) was detected to be 0.14 ns (Figure S4). Anchoring hexahedron prism allows for the longer survive time of the electron of CP1 of 0.16 ns and CP2 of 1.24 ns, decreasing recombination opportunity of electron and hole.

To experimentally prove the redox reaction to take place separately on the {111} and {100} facets under photo-illumination, the Pt reduction and MnO_x oxidation cocatalysts were photodeposited on CP2. The typical TEM image of the loaded Pt shows that over 90% of Pt tiny particles with ~5 nm prefers to densely coat on the octahedron surface and sparsely on the hexahedron prism (Figure S5a,b). Sponge-like manganese oxide deposits are formed selectively on the hexahedron prism instead of the octahedron (Figure S5c,d). This observation implies that the photogenerated electrons are readily available for the reduction on the {111} facets and the holes for oxidation on the {100}.

The carrier mobility of the different crystal facets, {111} and {100} faces, is another important factor to understand the activity differences in CH_4 generation among various CeO_2 faceted homojunctions. It is well-known that if the carrier effective mass is lighter, the carriers will have more probability of reaching the surface reactive sites within their lifetime.[24] The carrier effective mass is calculated by the following formula,[32] $E(k) = h^2k^2/2m_n$ (where E is the band energy, k is the wave vector, h is the Planck constant, and m_n is the carrier effective mass). This equation clearly shows that the different atom distributions of exposed crystal surfaces will engender different energy band structures and thus have a different carrier effective mass. Our generalized gradient approximation (GGA) functional calculations showed that the hole effective mass for the {111} and {100} facets were $1.140m_0$ and $1.031m_0$ (m_0 is the mass of free electron), and the electron effective mass of $3.333m_0$ and $8.376m_0$ (Figure S6 and Table S1). The electron mass along {111} is over 2 times smaller than that on {100}, therefore making electron migration toward {111} facets much more straightforward than {100} and thus decreasing the probability of recombination. Meanwhile, the hole mass along {100} is also smaller compared to {111}, indicating that the hole migration toward {100} facets is greatly encouraged.

In conclusion, the CeO_2 facet-based homojunction consisting of hexahedron-prism anchored CeO_2 octahedron core was synthesized for photocatalytic reduction of CO_2 into methane. The unique hierarchical nanostructure is spontaneously propitious to the spatial separation of the photogenerated carries, charge transfer, and selected redox facets, which extensively improves the CH_4 generation efficiency.

■ ASSOCIATED CONTENT

Ⓢ Supporting Information

Experimental details, XRD spectra, UV spectra, photoluminescence decay spectra, SEM, and DFT calculation data. The Supporting Information is available free of charge on the ACS Publications website at DOI: 10.1021/jacs.5b05926.

■ AUTHOR INFORMATION

Corresponding Authors

*zhouyong1999@nju.edu.cn
*zgzou@nju.edu.cn

Notes

The authors declare no competing financial interest.

■ ACKNOWLEDGMENTS

■ REFERENCES

(1) Wen, F. Y.; Li, C. *Acc. Chem. Res.* **2013**, *46*, 2355.
(2) Liu, G.; Yang, H. G.; Pan, J.; Yang, Y. Q.; Lu, G. Q.; Cheng, H. M. *Chem. Rev.* **2014**, *114*, 9559.
(3) Li, R.; Zhang, F.; Wang, D.; Yang, J.; Li, M.; Zhu, J.; Zhou, X.; Han, H.; Li, C. *Nat. Commun.* **2013**, *4*, 1432.
(4) Huang, W. C.; Lyu, L. M.; Yang, Y. C.; Huang, M. H. *J. Am. Chem. Soc.* **2012**, *134*, 1261.
(5) Wang, L.; Ge, J.; Wang, A.; Deng, M.; Wang, X.; Bai, S.; Li, R.; Jiang, J.; Zhang, Q.; Luo, Y.; Xiong, Y. *Angew. Chem., Int. Ed.* **2014**, *53*, 5107.
(6) Yang, P. D. *Nature* **2011**, *482*, 41.
(7) Bi, Y.; Ouyang, S.; Umezawa, N.; Cao, J.; Ye, J. *J. Am. Chem. Soc.* **2011**, *133*, 6490.
(8) Yi, Z.; Ye, J.; Kikugawa, N.; Kako, T.; Ouyang, S.; Williams, H.; Yang, H.; Cao, J.; Luo, W.; Li, Z.; Liu, J.; Withers, R. *Nat. Mater.* **2010**, *9*, 559.
(9) Martin, D. J.; Umezawa, N.; Chen, X.; Ye, J.; Tang, J. *Energy Environ. Sci.* **2013**, *6*, 3380.
(10) Jiang, J.; Zhao, K.; Xiao, X.; Zhang, L. *J. Am. Chem. Soc.* **2012**, *134*, 4473.
(11) Guan, M.; Xiao, C.; Zhang, J.; Fan, S.; An, R.; Cheng, Q.; Xie, J.; Zhou, M.; Ye, B.; Xie, Y. *J. Am. Chem. Soc.* **2013**, *135*, 10411.
(12) Cargnello, M.; Gordon, T. R.; Murray, C. B. *Chem. Rev.* **2014**, *114*, 9319.
(13) Li, R.; Han, H.; Zhang, F.; Wang, D.; Li, C. *Energy Environ. Sci.* **2014**, *7*, 1369.
(14) Li, H.; Zhou, Y.; Tu, W.; Ye, J.; Zou, Z. *Adv. Funct. Mater.* **2015**, *25*, 998.
(15) Wang, X.; Xu, Q.; Li, M.; Shen, S.; Wang, X.; Wang, Y.; Feng, Z.; Shi, J.; Han, H.; Li, C. *Angew. Chem., Int. Ed.* **2012**, *51*, 13089.
(16) Elias, J. S.; Risch, M.; Giordano, L.; Mansour, A. N.; Shao-Horn, Y. *J. Am. Chem. Soc.* **2014**, *136*, 17193.
(17) Yu, T.; Zeng, J.; Lim, B.; Xia, Y. *Adv. Mater.* **2010**, *22*, 5188.
(18) Vile, G.; Colussi, S.; Krumeich, F.; Trovarelli, A.; Perez-Ramirez, J. *Angew. Chem., Int. Ed.* **2014**, *53*, 12069.
(19) Primo, A.; Marino, T.; Corma, A.; Molinari, R.; Garcia, H. *J. Am. Chem. Soc.* **2011**, *133*, 6930.
(20) Chueh, W.; Falter, C.; Abbott, M.; Scipio, D.; Furler, P.; Haile, S.; Steinfeld, A. *Science* **2010**, *330*, 1797.
(21) Baudin, M.; Wojcik, M.; Hermansson, K. *Surf. Sci.* **2000**, *468*, 51.
(22) Nolan, M.; Grigoleit, S.; Sayle, D. C.; Parker, S. C.; Watson, G. W. *Surf. Sci.* **2005**, *576*, 217.
(23) Nolan, M.; Watson, G. *J. Phys. Chem. B* **2006**, *110*, 16600.
(24) Yan, L.; Yu, R.; Chen, J.; Xing, X. *Cryst. Growth Des.* **2008**, *8*, 1474.
(25) Li, Z.; Zhou, Y.; Zhang, J.; Tu, W.; Liu, Q.; Yu, T.; Zou, Z. *Cryst. Growth Des.* **2012**, *12*, 1476.
(26) Bao, L.; Yang, H.; Wang, X.; Zhang, F.; Shi, R.; Liu, B.; Wang, L.; Zhao, H. *J. Cryst. Growth* **2011**, *328*, 62.
(27) Kuchibhatla, S. V.; Karakoti, A. S.; Seal, S. *Nanotechnology* **2007**, *18*, 075303.
(28) Wang, Z.; Feng, X. *J. Phys. Chem. B* **2003**, *107*, 13563.
(29) Wang, Z. *J. Phys. Chem. B* **2000**, *104*, 1153.
(30) Roh, J.; Hwang, S. H.; Jang, J. *ACS Appl. Mater. Interfaces* **2014**, *6*, 19825.
(31) Liu, Q.; Zhou, Y.; Kou, J.; Chen, X.; Tian, Z.; Gao, J.; Yan, S.; Zou, Z. *J. Am. Chem. Soc.* **2010**, *132*, 14385.
(32) Yan, S. C.; Ouyang, S. X.; Gao, J.; Yang, M.; Feng, J. Y.; Fan, X. X.; Wan, L. J.; Li, Z. S.; Ye, J. H.; Zhou, Y.; Zou, Z. G. *Angew. Chem.* **2010**, *122*, 6544.
(33) Tu, W.; Zhou, Y.; Liu, Q.; Tian, Z.; Gao, J.; Chen, X.; Zhang, H.; Liu, J.; Zou, Z. *Adv. Funct. Mater.* **2012**, *22*, 1215.
(34) Tu, W.; Zhou, Y.; Zou, Z. *Adv. Funct. Mater.* **2013**, *23*, 4996.
(35) Gaulding, E. A.; Diroll, B. T.; Goodwin, E. D.; Vrtis, Z. J.; Kagan, C. R.; Murray, C. B. *Adv. Mater.* **2015**, *27*, 2846.
(36) Yu, J. G.; Low, J. X.; Xiao, W.; Zhou, P.; Jaroniec, M. *J. Am. Chem. Soc.* **2014**, *136*, 8839.